Draft version December 16, 2025
Typeset using LaTeX twocolumn style in AASTeX631

High-Redshift Galaxy Candidates at $z = 6+$ as Revealed by *JWST* Observations of MACS0647

Keduse Worku,[1,2] Tiger Yu-Yang Hsiao,[3,4] Dan Coe,[2,5,1] Abdurro'uf,[6,1,2] Tom Resseguier,[1,2] Rebecca L. Larson,[7] Jacqueline Antwi-Danso,[8] Gabriel Brammer,[9,10] Vasily Kokorev,[4] Larry D. Bradley,[2] Lukas J. Furtak,[3,4] and Masamune Oguri[11,12]

[1] *Center for Astrophysical Sciences, Department of Physics and Astronomy, The Johns Hopkins University, 3400 N Charles St. Baltimore, MD 21218, USA*
[2] *Space Telescope Science Institute (STScI), 3700 San Martin Drive, Baltimore, MD 21218, USA*
[3] *Cosmic Frontier Center, The University of Texas at Austin, Austin, TX 78712, USA*
[4] *Department of Astronomy, The University of Texas at Austin, Austin, TX 78712, USA*
[5] *Association of Universities for Research in Astronomy (AURA), Inc. for the European Space Agency (ESA)*
[6] *Department of Astronomy, Indiana University, 727 East Third Street, Bloomington, IN 47405, USA*
[7] *School of Physics and Astronomy, Rochester Institute of Technology, 84 Lomb Memorial Drive, Rochester, NY 14623, USA*
[8] *David A. Dunlap Department of Astronomy and Astrophysics, University of Toronto, 50 St. George Street, Toronto, Ontario, M5S 3H4, Canada**
[9] *Cosmic Dawn Center (DAWN), Copenhagen, Denmark*
[10] *Niels Bohr Institute, University of Copenhagen, Jagtvej 128, Copenhagen, Denmark*
[11] *Center for Frontier Science, Chiba University, 1-33 Yayoi-cho, Inage-ku, Chiba 263-8522, Japan*
[12] *Department of Physics, Graduate School of Science, Chiba University, 1-33 Yayoi-Cho, Inage-Ku, Chiba 263-8522, Japan*

ABSTRACT

We present a catalog of 57 high-redshift $z > 6$ galaxy candidates, including 14 spectroscopic confirmations ($z = 6.10 - 9.25$), 2 Little Red Dots ($z = 4.77$, 5.81), and 2 interlopers ($z = 3.23$, 3.72), based on *JWST* NIRCam imaging (7 filters), NIRSpec spectroscopy (PRISM and G395H), and archival *HST* imaging (17 filters) of the strong lensing galaxy cluster MACS0647. Our highest redshift confirmation ($z = 9.25$) is an Extremely Blue Galaxy (presented in Yanagisawa et al. 2024), and here we identify a spectral turnover likely due to damped Lyman-α. We identify an overdensity of galaxies with spectroscopic redshifts $z = 6.1$, confirming the $z \sim 6$ overdensity identified in *HST* images. In one of these galaxies, our high-resolution G395H spectroscopy reveals two spatially resolved components with a velocity difference of ∼90 km/s; if these components are gravitationally bound, this would imply a dynamical mass on the order of $\sim 10^8\ M_\odot$ given their projected separation. We present spectral line fluxes, widths, and derived physical properties, including stellar masses ($10^8 - 10^9$ M$_\odot$) and metallicities (10%−40% Z$_\odot$) for our spectroscopic sample. We note half of our NIRSpec data was obtained with standard 3-slitlet nods and half was obtained with single slitlets yielding similar results, demonstrating the power to observe more sources on a densely packed NIRSpec MSA.

1. INTRODUCTION

A significant phase transition occurred in the Intergalactic Medium (IGM) as it shifted from a neutral to an ionized state at $z \sim 6$ (about 1 Gyr after the Big Bang), marking the period known as the Epoch of Reionization (EoR; Loeb & Barkana 2001). The culprits behind this reionization phase are widely believed to be the intense UV radiation emitted by the first generation of galaxies and stars (e.g., Fan et al. 2006; Bouwens et al. 2012; Duncan & Conselice 2015; Dayal & Ferrara 2018; Naidu et al. 2020). The crucial task of detecting and characterizing galaxies at high redshifts becomes paramount in comprehending the evolutionary trajectory of galaxies, as well as in gaining insight into the mechanisms behind the EoR (e.g., Robertson 2022). However, our ability to study early galaxies remains constrained by the limitations in telescope sensitivity.

Thanks to the advanced capabilities of the *JWST* (Gardner et al. 2006) a multitude of galaxies with redshifts > 10 have been brought to light through photometric discovery utilizing NIRCam (Rigby et al. 2022;

Corresponding author: Keduse Worku
kworku2@jhu.edu

* Banting Postdoctoral Fellow

Harikane et al. 2022; Castellano et al. 2022; Bradley et al. 2022; Naidu et al. 2022a; Finkelstein et al. 2022; Yan et al. 2023; Adams et al. 2023; Whitler et al. 2023; Donnan et al. 2023; Atek et al. 2023; Harikane et al. 2023; Hsiao et al. 2023a; Casey et al. 2023). This impressive feat has been complemented by spectroscopic confirmations facilitated by NIRSpec (e.g., Kokorev et al. 2025; Pérez-González et al. 2025; Castellano et al. 2025; Curtis-Lake et al. 2023; Wang et al. 2023; Hsiao et al. 2023b; Goulding et al. 2023), including the identification of two compelling galaxies with redshifts surpassing 13 (Naidu et al. 2025; Wu et al. 2025; Carniani et al. 2024; Curtis-Lake et al. 2023; Wang et al. 2023). This collection of unparalleled data has granted us the opportunity to delve into an array of studies encompassing luminosity functions (e.g., Donnan et al. 2024, 2023; Harikane et al. 2023), stellar masses (e.g., Hsiao et al. 2023a; Mowla et al. 2024), star-formation histories (e.g., Hsiao et al. 2023a), cosmic star formation history (e.g., Harikane et al. 2023), as well as Lyman-alpha damping wings (e.g., Hsiao et al. 2023b; Heintz et al. 2023, 2025a) within the context of the high-redshift universe.

Gravitational lensing induced by massive galaxy clusters serves to magnify both the light emitted by distant objects and their physical dimensions. This cosmic telescope not only brings the fluxes of faint objects from the early Universe into the observable range, but also enhances the visibility of small-scale structures (e.g., Coe et al. 2013; Welch et al. 2022a; Vanzella et al. 2022; Meštrić et al. 2022; Welch et al. 2022b,c; Claeyssens et al. 2023; Hsiao et al. 2023a; Fujimoto et al. 2024; Mowla et al. 2024; Adamo et al. 2024; Nightingale et al. 2025). Consequently, gravitational lensing has enabled us to unveil and scrutinize early galaxies along with their intrinsic properties. In pursuit of investigating numerous pivotal scientific inquiries pertaining to the early Universe, a variety of surveys centered around lensing clusters have been undertaken. These initiatives encompass the Cluster Lensing and Supernova survey with Hubble[1] (CLASH; Postman et al. 2012), the Hubble Frontier Fields project (Lotz et al. 2017), and the Reionization Lensing Cluster Survey[2] (RELICS; Coe et al. 2019).

CLASH stands as one of the significant Hubble treasury programs that has embraced the lensing technique for the exploration of distant galaxies (e.g., Zheng et al. 2012; Coe et al. 2013; Bouwens et al. 2014; Smit et al. 2014; Bradley et al. 2014). This initiative captured imagery of 25 massive galaxy clusters across 16 filters using the *HST*, spanning a wavelength range from the near-ultraviolet ($\sim 200\,$nm) to the near-infrared ($\sim 1.6\,\mu$m), with inclusion of the galaxy cluster MACSJ0647.7+7015 (MACS0647; $z = 0.591$) (Ebeling et al. 2007) modeled by (Zitrin et al. 2011). Through CLASH observations, Bradley et al. (2014) identified 32 lensed candidates at redshifts around $z \sim 6$ to 8. In addition, a triply-lensed candidate with a redshift of approximately $z \sim 11$, named MACS0647–JD, was discovered in the same field (Coe et al. 2013). Furthermore, *JWST*/NIRCam observations unveiled the intricate structure of MACS0647–JD, resolving it into two components down to a scale of 20 pc (Hsiao et al. 2023a). Subsequent *JWST*/NIRSpec observations confirmed the redshift of MACS0647–JD to be $z = 10.17$ and revealed seven emission lines (Hsiao et al. 2023b). In particular, *JWST* observations of MACS0647 also identified two potential lensed stars with a redshift of $z = 4.76$ (Meena et al. 2023; Furtak et al. 2024).

Despite the numerous high-z candidates unveiled by *JWST*, a peculiar case of misclassification involving the galaxy CEERS-93316 emerges. This galaxy, initially assigned a photometric redshift of $z = 16$ (Donnan et al. 2023), has since been validated at a spectroscopic redshift of $z = 4.9$ as indicated by Arrabal Haro et al. (2023) due to its pronounced emission lines. In particular, galaxies with robust optical nebular emission lines at $z < 6$ can mimic the NIRCam photometric profiles of $z > 7-10$ Lyman Break Galaxies (e.g., McKinney et al. 2023). Furthermore, the issue of dusty galaxies has long posed a significant challenge in tainting high redshift galaxy observations within photometric data, a predicament predating the era of *JWST* (e.g., Naidu et al. 2022b). Thus, the confirmation of redshifts demands complementary spectroscopic follow-up investigations. This potential quandary may perplex astronomers as the era of *JWST*, *Euclid*, and the Roman Space Telescope yields unparalleled photometric data, yet remains constrained by a scarcity of spectroscopic data (Rigby et al. 2022; Mellier & et al. 2025; Eifler et al. 2021).

In this work, we present and analyze a sample of approximately 50 galaxy candidates at a redshift of $z > 6$ in the recent observations of MACS0647 using 7 *JWST* NIRCam filters ($1.15 - 5\,\mu$m). We investigate their early galaxy evolution through detailed physical characterizations, such as stellar masses and dust content, while constraining their star formation history. Furthermore, we spectroscopically confirmed 15 of these galaxies through JWST NIRSpec data with Hi-Res and prism modes (including MACS0647–JD; see also Hsiao et al. 2023b; Abdurro'uf et al. 2024), additionally revealing two low-

[1] https://www.stsci.edu/~postman/CLASH/

[2] https://relics.stsci.edu

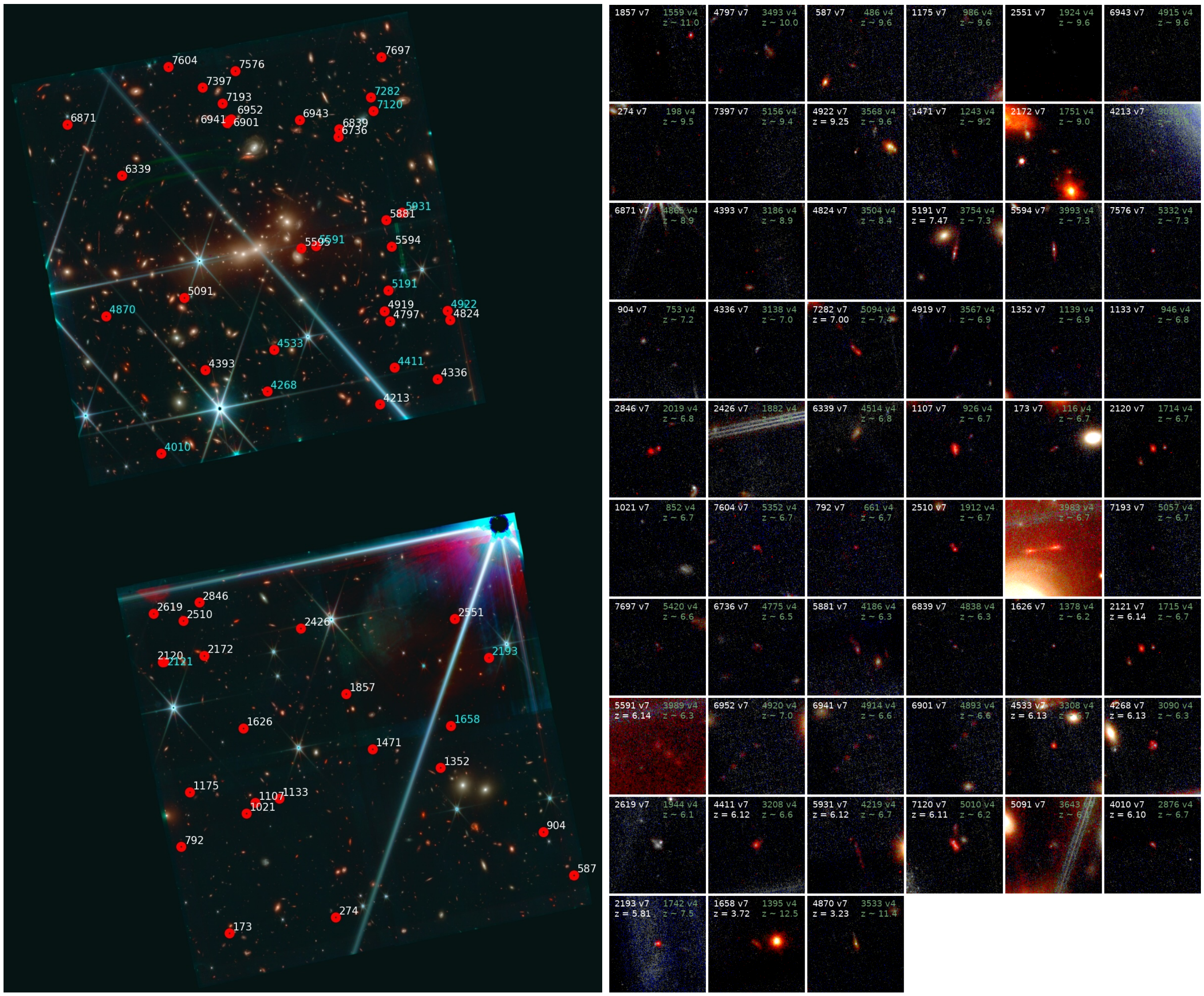

Figure 1. Left: Overview MACS0647 NIRCam color image based on DJA v7 reductions of observations in six wide filters. High-redshift candidates are labeled in white (v7 ID numbers), while galaxies with spectroscopic redshifts are indicated in cyan. **Right:** *JWST* NIRCam $4'' \times 4''$ color images, each centered on a high-redshift candidate in the final sample.

redshift interlopers. Candidates of note include strong Lyman $-\alpha$ emitters, a Little Red Dot (LRD), and an overdensity of galaxies at $z = 6.1$, indicating possible cluster islands of reionization.

This paper is organized as follows: Section §2 details the *JWST* and *HST* observational datasets and data reduction; Section §3 describes our methodology, including our photometric and spectroscopic analysis with high-redshift galaxy selection detailed in §3.1; we delve into a comprehensive discussion of our findings in Section §4, which encompass measurements of physical parameters derived from SED and spectroscopic fitting; finally, Section §5 provides our concluding remarks.

2. DATA

We utilize NIRCam imaging and NIRSpec prism spectroscopy data from the *JWST* Cycle 1 program GO 1433 (PI Coe; Hsiao et al. 2023a) and NIRSpec G395H high-resolution spectra from the *JWST* Cycle 2 program GO 4246 (PI Abdurro'uf; Abdurro'uf et al. 2024). We also combine the imaging data with the archival *HST* imaging from programs GO 9722, 10493, 10793, 12101, and 13317. A thorough description of these data sets is given in Hsiao et al. (2023a,b); Abdurro'uf et al. (2024). In the following, we will only briefly describe some of the data that are used in the analysis of this paper.

2.1. *HST imaging*

MACS0647+70 was observed through 39 *HST* orbits across 17 different filters. Its initial observations were

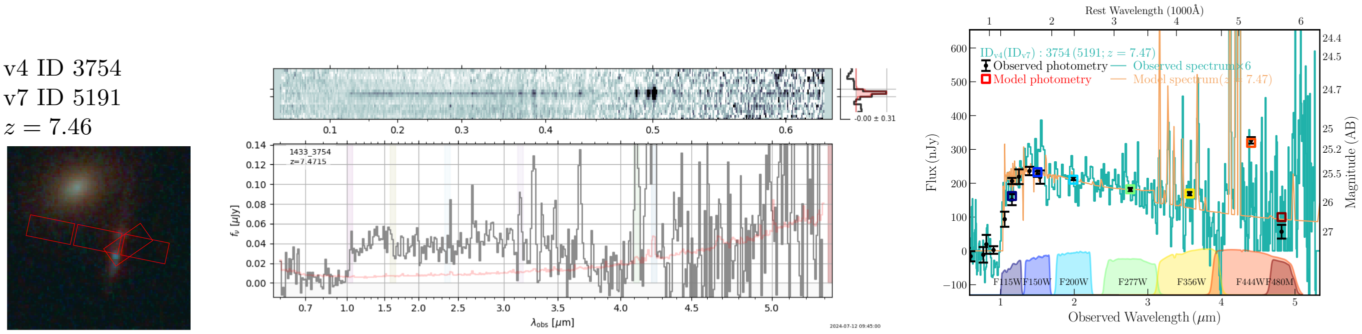

Figure 2. Example of a high-redshift galaxy (v4 3754 / v7 5191, $z = 7.464$) observed with NIRSpec PRISM in both Cycle 1 slitlet configurations. This target was observed in Obs 21 using single-slitlet placements and in Obs 23 using the standard 3-slitlet nod pattern (left). The PRISM spectrum (middle) shows multiple strong emission lines, and the corresponding SED fit is shown on the right.

carried out as part of programs GO 9722 (PI Ebeling), and GO 10493 and 10793 (PI Gal-Yam), employing the ACS F555W and F814W filters. Subsequently, the CLASH program (GO 12101, PI Postman) extended the observations by employing 15 additional filters spanning a wavelength range from 0.2 to 1.7 micrometers, utilizing the WFC3/UVIS, ACS, and WFC3/IR instruments. Furthermore, supplementary imaging in the WFC3/IR F140W filter was acquired as part of a grism spectroscopy program (GO 13317, PI Coe).

2.2. *JWST NIRCam imaging*

JWST NIRCam imaging was obtained using 6 filters: F115W, F150W, F200W, F277W, F356W, and F444W, spanning the wavelength range of $1 - 5\,\mu$m. Subsequently, additional NIRCam imaging was obtained in the F200W and F480M filters, concurrently with the NIRSpec observation 21 (Obs 21), as detailed in §2.3. Each NIRCam image involved a 35-minute exposure time, distributed across 4 INTRAMODULEBOX dithers to cover short-wavelength gaps. For an in-depth understanding of the reduction process, we direct interested readers to consult Hsiao et al. (2023a,b). In brief, the NIRCam images underwent processing through the GRIZLI pipeline (Brammer et al. 2022). Initially, GRIZLI v4 images were employed for high-redshift candidate selection (see §3.1). Updated zeropoint corrections, based on refined calibrations, were implemented in GRIZLI v5. In this study, we conducted our analysis using GRIZLI v7 image mosaics, which featured improved sky flats, bad pixel tables, wisp templates, and long-wavelength zeropoints.

Figure 1 shows the NIRCam color composite of MACS0647 used to identify and label the high-redshift candidates in this work, alongside each individual galaxy candidate.

2.3. *JWST NIRSpec spectroscopy*

The *JWST* Cycle 1 (GO 1433) NIRSpec multi-object spectroscopy (MOS) observation using the microshutter assembly (MSA) was conducted on 2023-01-08 (Obs 21) and 2023-02-20 (Obs 23). Both used the low resolution $R \sim 30-300$ prism that covers a wide wavelength range from $0.6 - 5.3\,\mu$m. Obs 21 was performed with single slitlets (plus two dithers), while Obs 23 was performed with standard 3-slitlet nods. The two observations have a similar exposure time of 1.8 hours. Twenty high redshift candidates (see §3.1), including MACS0647−JD (Hsiao et al. 2023b), were selected to be observed with NIRSpec based on their photometric redshifts (see also Table 2), with the spectra of ten candidates allowing us to determine their spectroscopic redshift.

In *JWST* Cycle 2 (GO 4246), we obtained NIRSpec MOS G395H (2.9 – 5.3μm) high-resolution ($R \sim 3000$) spectra on 2024-01-14. The standard 3-slitlet nods had a total exposure time of 2.5 hours. Representative G395H spectra are shown in Appendix A (Figures 6 and 7).

Our NIRSpec data reduction is described in (Abdurro'uf et al. 2024; Hsiao et al. 2024). Briefly, we retrieved NIRSpec Level 1 data products from MAST and processed them with the STScI *JWST* pipeline[3] and `msaexp`.[4] We retrieved reduced spectra from the Dawn JWST Archive (DJA)[5] and also reprocessed some separately.

For the PRISM data, we find the single-slitlet and 3-slitlet data yield similar results. Our NIRSpec PRISM data is unique in this respect: for some galaxies, we have both observations and can compare directly. For the single-slitlet data, we subtract backgrounds measured in nearby empty slits (added for this purpose). Single-slitlet observations allow more science targets to

[3] https://github.com/spacetelescope/jwst

[4] https://github.com/gbrammer/msaexp

[5] https://dawn-cph.github.io/dja/

be densely packed on the NIRSpec MSA. An example galaxy observed with both single-slitlet and 3-slitlet PRISM configurations is shown in Figure 2.

3. METHODS

3.1. *Candidate Selection*

To select candidates $z \geq 6$ from our sample, we use a combination of photometric redshift fitting using EAZY (described in Sec. 3.2) and significance of detection in band signals. The simultaneous analysis of all photometric bands in SED fitting and its extensive use in the literature allows for effective high-redshift candidate selection (Bradley et al. 2022; Finkelstein et al. 2022; Naidu et al. 2022c; Adams et al. 2023; Donnan et al. 2023; Finkelstein et al. 2023).

Our primary selection criteria are:

1. Signal-to-noise ratio ≥ 3 in the F356W band
2. Signal-to-noise ratio ≥ 3 in at least two other filters
3. Best-fit photometric redshift z ≥ 6

The signal-to-noise criteria across multiple photometric bands supports the robustness of candidate detections. Additionally, each filter image and best-fit SED was reviewed to eliminate diffraction spikes and instrument artifacts.

3.2. *Spectral Energy Distribution (SED) Fitting*

We completed the SED fitting through the analysis codes BAGPIPES (Bayesian Analysis of Galaxies for Physical Inference and Parameter EStimation) (Carnall et al. 2018) and EAZY (Easy and Accurate Z-photo from Yale) (Brammer et al. 2008) with redshift as a free parameter.

Our initial SED fitting was performed with EAZY, which features a non-negative linear combination of templates from HST, Spitzer, and JWST photometry. We use the FSPS (Flexible Stellar Population Synthesis) templates (Conroy & Gunn 2010) in the fitting. While these templates are widely used for high-redshift studies, they are calibrated primarily on low-redshift galaxies, and uncertainties in stellar population models at $z > 4$ can affect parameter estimates (Mobasher et al. 2015; Leja et al. 2019). To mitigate these uncertainties, we performed follow-up analysis with BAGPIPES.

BAGPIPES is a Bayesian spectral-fitting code that uses the MultiNest nested sampling algorithm (Feroz & Hobson 2008; Feroz et al. 2009; Feroz & Skilling 2013) implemented through the PyMultiNest interface (Buchner et al. 2014) to estimate galaxy properties from photometric and spectroscopic data. The stellar population synthesis modeling is based on the 2016 updated BC03 models (Bruzual & Charlot 2003), built on a Kroupa (Kroupa 2002) initial mass function (IMF).

For our SED fitting, we used two star formation histories, a constant star formation rate and a delayed exponentially declining SFH, where the star formation rate (SFR) is of the form $\mathrm{SFR}(t) \propto t\exp(-t/\tau)$. The constant SFH model often yields systematically younger ages, whereas the delayed-τ model is generally considered better suited for high-redshift candidates due to its ability to capture rising star formation histories expected in early galaxies (e.g., Papovich et al. 2011; Pacifici et al. 2013; Carnall et al. 2019). However, we include the constant SFH for straightforward comparison with previous studies in the literature. We assume a Small Magellanic Cloud (SMC) dust law (Salim et al. 2018), with dust extinction ranging between $A_V = 0 - 3$. The age varied between 1 Myr and the age of the universe, and the permitted metallicity ranges were $\log Z/Z_{\odot} = 0.005 - 5$.

3.3. *Spectral Fitting*

We measured emission line fluxes with MSAEXP, which jointly models continuum plus Gaussian emission lines for each spectrum. The resulting line flux measurements from the PRISM data and the G395H observations are reported in Tables 5 and 6, respectively.

4. RESULTS AND DISCUSSION

Based on SED fitting to the NIRCam photometry, we present estimates of physical parameters in Table 1. We then turn to the spectroscopy to measure properties in more detail.

4.1. *Spectroscopic Results*

In Table 7.2, we present the measured emission line fluxes for 9 galaxies observed with NIRSpec PRISM. A total of 20 emission lines were detected across these galaxies, with each galaxy exhibiting between 4 and 13 lines in their spectra. All galaxies in the sample have the [OIII] $\lambda5007$ line, an important tracer of star-formation. For four of the galaxies, we also report measurements of metallicity and the ionization parameter, providing additional constraints on their chemical composition and ionization states.

The physical properties inferred from both photometry and spectroscopy indicate a population of relatively low-mass, low-metallicity galaxies. We measure metallicities of $\sim$ 10–40% $Z_{\odot}$ and stellar masses between $\sim 10^8$ and $10^9\,M_{\odot}$. These values are broadly consistent with other recent studies of galaxies at $z > 6$ using JWST and ground-based spectroscopy (Curtis-Lake et al. 2023; Sanders et al. 2023; Cameron et al. 2024;

Table 1. Physical properties derived with BAGPIPES for a subset of our high-redshift candidates, based on NIRCam photometry and multi-band SED fitting. **Note:** Little Red Dots (LRDs) are marked with an asterisk (*); their SED fits may be unreliable due to extreme colors or AGN contamination.

ID (v7)	ID (v4)	$z_{\rm phot}$	Stellar Mass $\log(M_*/M_\odot)$	SFR $(M_*/{\rm yr})$	sSFR $({\rm yr}^{-1})$	A_V (mag)	Mass-weighted Age (Myr)
173	116	$6.30^{+0.52}_{-5.14}$	$8.58^{+0.25}_{-0.94}$	$2.74^{+2.00}_{-2.67}$	$-8.27^{+0.30}_{-0.54}$	$0.23^{+0.28}_{-0.14}$	162^{+430}_{-85}
1107	926	$6.58^{+0.15}_{-0.12}$	$9.12^{+0.14}_{-0.14}$	$49.28^{+5.22}_{-3.81}$	$-7.40^{+0.12}_{-0.16}$	$0.51^{+0.04}_{-0.03}$	17^{+9}_{-5}
1352	1139	$6.93^{+0.74}_{-4.78}$	$8.54^{+0.17}_{-0.62}$	$1.94^{+1.49}_{-1.80}$	$-8.31^{+0.24}_{-0.25}$	$0.32^{+0.23}_{-0.15}$	177^{+139}_{-79}
2120	1714	$6.69^{+0.03}_{-0.04}$	$8.88^{+0.06}_{-0.09}$	$24.93^{+3.85}_{-2.74}$	$-7.47^{+0.09}_{-0.10}$	$0.54^{+0.04}_{-0.04}$	21^{+6}_{-5}
2193*	1742	$7.19^{+0.08}_{-0.09}$	$10.04^{+0.04}_{-0.03}$	$39.10^{+5.99}_{-15.60}$	$-8.44^{+0.06}_{-0.27}$	$0.70^{+0.05}_{-0.14}$	240^{+56}_{-32}
2510	1912	$6.72^{+0.05}_{-0.08}$	$8.99^{+0.13}_{-0.14}$	$13.13^{+3.13}_{-3.74}$	$-7.87^{+0.22}_{-0.27}$	$0.43^{+0.06}_{-0.07}$	58^{+58}_{-25}
2619	1944	$6.81^{+0.03}_{-0.03}$	$9.90^{+0.03}_{-0.03}$	$29.45^{+3.28}_{-2.00}$	$-8.44^{+0.07}_{-0.04}$	$0.41^{+0.03}_{-0.03}$	239^{+23}_{-39}
2846	2019	$6.49^{+0.36}_{-0.19}$	$9.08^{+0.11}_{-0.11}$	$5.26^{+2.14}_{-1.03}$	$-8.38^{+0.18}_{-0.10}$	$0.36^{+0.12}_{-0.08}$	207^{+56}_{-72}
4010	2876	$6.97^{+0.19}_{-0.17}$	$8.90^{+0.08}_{-0.12}$	$3.90^{+1.28}_{-0.82}$	$-8.32^{+0.21}_{-0.11}$	$0.13^{+0.09}_{-0.07}$	184^{+51}_{-76}
4213	3035	$7.67^{+0.40}_{-0.31}$	$7.82^{+0.26}_{-0.24}$	$1.61^{+0.41}_{-0.33}$	$-7.61^{+0.30}_{-0.34}$	$0.02^{+0.04}_{-0.02}$	30^{+42}_{-17}
4336	3138	$7.62^{+0.13}_{-0.13}$	$8.09^{+0.11}_{-0.11}$	$2.88^{+0.18}_{-0.20}$	$-7.62^{+0.11}_{-0.15}$	$0.01^{+0.01}_{-0.01}$	31^{+14}_{-8}
4411	3208	$6.61^{+0.01}_{-0.02}$	$9.06^{+0.06}_{-0.06}$	$28.03^{+4.15}_{-4.08}$	$-7.61^{+0.10}_{-0.10}$	$0.36^{+0.03}_{-0.03}$	30^{+9}_{-7}
4797	3493	$9.95^{+0.40}_{-0.32}$	$8.17^{+0.22}_{-0.25}$	$2.05^{+0.70}_{-0.41}$	$-7.86^{+0.31}_{-0.27}$	$0.06^{+0.10}_{-0.04}$	58^{+53}_{-32}
4922	3568	$9.67^{+0.23}_{-0.23}$	$8.11^{+0.17}_{-0.15}$	$2.59^{+0.49}_{-0.52}$	$-7.70^{+0.20}_{-0.22}$	$0.01^{+0.02}_{-0.01}$	38^{+27}_{-16}
5191	3754	$7.68^{+0.11}_{-0.10}$	$8.37^{+0.06}_{-0.05}$	$23.70^{+3.59}_{-2.72}$	$-7.00^{+0.00}_{-0.00}$	$0.11^{+0.03}_{-0.04}$	2^{+0}_{-0}
5591	3989	$6.31^{+0.22}_{-4.39}$	$8.07^{+0.18}_{-0.49}$	$0.68^{+0.47}_{-0.57}$	$-8.30^{+0.31}_{-0.23}$	$0.30^{+0.36}_{-0.19}$	172^{+122}_{-92}
5881	4186	$6.76^{+0.27}_{-0.11}$	$8.73^{+0.13}_{-0.14}$	$7.73^{+1.20}_{-0.97}$	$-7.84^{+0.19}_{-0.18}$	$0.02^{+0.03}_{-0.01}$	55^{+30}_{-22}
5931	4219	$6.77^{+0.50}_{-0.31}$	$7.52^{+0.18}_{-0.26}$	$0.23^{+0.09}_{-0.06}$	$-8.17^{+0.33}_{-0.23}$	$0.10^{+0.13}_{-0.07}$	127^{+96}_{-72}
6736	4775	$6.93^{+0.17}_{-0.19}$	$8.71^{+0.09}_{-0.12}$	$2.91^{+0.71}_{-0.41}$	$-8.24^{+0.20}_{-0.15}$	$0.05^{+0.06}_{-0.04}$	151^{+63}_{-60}
6839	4838	$6.69^{+0.16}_{-0.09}$	$8.72^{+0.11}_{-0.16}$	$3.09^{+0.91}_{-0.46}$	$-8.21^{+0.22}_{-0.18}$	$0.05^{+0.06}_{-0.04}$	139^{+77}_{-59}
6901	4893	$6.81^{+0.29}_{-0.21}$	$8.62^{+0.11}_{-0.16}$	$2.18^{+0.95}_{-0.55}$	$-8.27^{+0.23}_{-0.15}$	$0.15^{+0.12}_{-0.09}$	162^{+71}_{-70}
6941	4914	$6.88^{+0.50}_{-5.57}$	$8.60^{+0.14}_{-0.92}$	$2.47^{+2.02}_{-2.43}$	$-8.29^{+0.31}_{-0.63}$	$0.40^{+0.60}_{-0.17}$	167^{+604}_{-90}
7120	5010	$6.55^{+0.02}_{-0.02}$	$8.98^{+0.08}_{-0.10}$	$38.57^{+8.65}_{-3.64}$	$-7.37^{+0.07}_{-0.08}$	$0.32^{+0.05}_{-0.03}$	16^{+4}_{-3}
7282	5094	$7.21^{+0.12}_{-0.12}$	$8.78^{+0.08}_{-0.14}$	$7.00^{+1.98}_{-1.76}$	$-7.93^{+0.24}_{-0.19}$	$0.16^{+0.05}_{-0.06}$	67^{+41}_{-31}
7576	5332	$7.28^{+0.13}_{-0.12}$	$7.50^{+0.26}_{-0.21}$	$2.38^{+0.39}_{-0.45}$	$-7.06^{+0.06}_{-0.32}$	$0.03^{+0.04}_{-0.02}$	6^{+10}_{-4}
7604	5352	$6.48^{+0.04}_{-0.07}$	$8.36^{+0.18}_{-0.20}$	$7.99^{+1.14}_{-1.08}$	$-7.44^{+0.19}_{-0.22}$	$0.29^{+0.06}_{-0.04}$	19^{+14}_{-8}
7697	5420	$7.08^{+0.23}_{-0.19}$	$8.61^{+0.09}_{-0.16}$	$2.37^{+0.80}_{-0.45}$	$-8.24^{+0.24}_{-0.16}$	$0.08^{+0.07}_{-0.05}$	147^{+72}_{-67}

Hainline et al. 2024a; Heintz et al. 2025b). The low metallicities reflect the limited time for chemical enrichment in the early universe, while the stellar masses and star formation rates indicate that our sample includes both relatively young, intensely star-forming systems and more quiescent objects. The SFRs derived from our SED fits also span a wide range, suggesting a diversity of evolutionary stages among the high-redshift population.

It is important to note that our spectroscopic sample is subject to selection effects. The NIRSpec targets were chosen based on photometric redshift and brightness criteria, which preferentially select galaxies with strong rest-optical emission lines or prominent breaks. This selection can bias the sample toward actively star-forming or less dusty galaxies, and the physical properties we derive may not be fully representative of the underlying population of all $z > 6$ galaxies in the field (Tang et al. 2024; Rhoads et al. 2023). Additionally, uncertainties in lensing magnification factors, particularly for multiply imaged sources, can affect the intrinsic luminosities and derived physical parameters (Welch et al. 2022a; Meena et al. 2023).

4.2. *Extremely Blue Galaxy EBG-1 at $z = 9.25$*

Our highest-redshift galaxy, v4 3568 (v7 4922), lies at $z = 9.25$ and was previously identified as EBG-1 by Yanagisawa et al. (2024). This "extremely blue galaxy" ($\beta = -3.0$) is inferred to have a high ionizing photon escape fraction, $f_{\rm esc}^{\rm ion} > 0.5$, suggesting vigorous, low-metallicity star formation. Figure 4 presents the NIRCam imaging, NIRSpec PRISM spectroscopy, and SED fit for EBG-1.

In our analysis, the JWST spectrum exhibits a turnover in F_ν that may arise from either damped Lyα

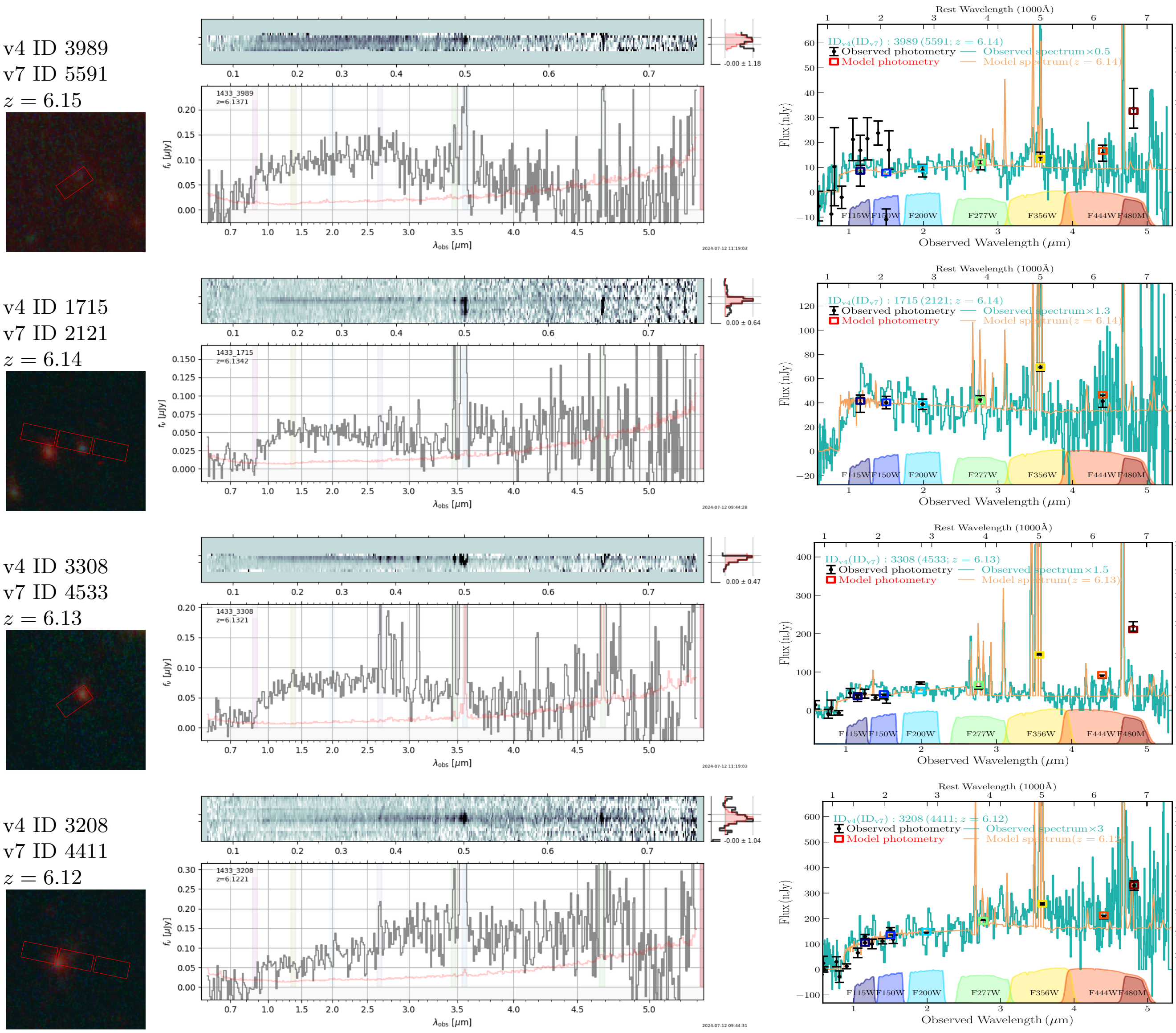

Figure 3. Four example members of the overdensity at $6.12 < z < 6.15$ identified with NIRSpec PRISM. For each galaxy we show **Left:** the NIRCam color image with slit orientation, **Middle:** the 2D and 1D PRISM spectra, and **Right:** the NIRCam photometry together with the SED model constrained by the spectrum. These sources, together with five additional galaxies in the same narrow redshift slice, indicate a prominent overdensity at $z \sim 6.1$ behind MACS0647.

absorption (Heintz et al. 2024) or two-photon continuum emission associated with a young, metal-poor stellar population and a top-heavy IMF (Cameron et al. 2024). Both scenarios point to an early, rapidly evolving system.

EBG-1 is only modestly magnified in our lensing model, with $\mu \approx 2.7$ (Table 3), indicating that its extreme UV slope and high inferred escape fraction are intrinsic properties rather than artifacts of strong lensing. This makes EBG-1 one of the most compelling $z > 9$ galaxies in the field, and a prime target for future spectroscopic and radiative-transfer studies.

4.3. *High-redshift $z \sim 7$ galaxies*

We confirm two galaxies at $z \sim 7$. v4 3754 (v7 5191) at $z = 7.464$ features many emission lines in the PRISM data. [O III] and Hβ are also detected with G395H. v4 5094 (v7 7282) is confirmed at $z = 6.997$ with G395H detections of [O III], [Ne III], and [O II]. We include the G395H spectra of v4 3754 (v7 5191) within the Appendix A (see Figure 6).

4.4. *Overdensity at $z = 6.1$*

We detect an overdensity of galaxies at $z = 6.1$. We confirm 9 galaxies spectroscopically with $6.11 < z < 6.15$ in our PRISM and G395H observations (Figures

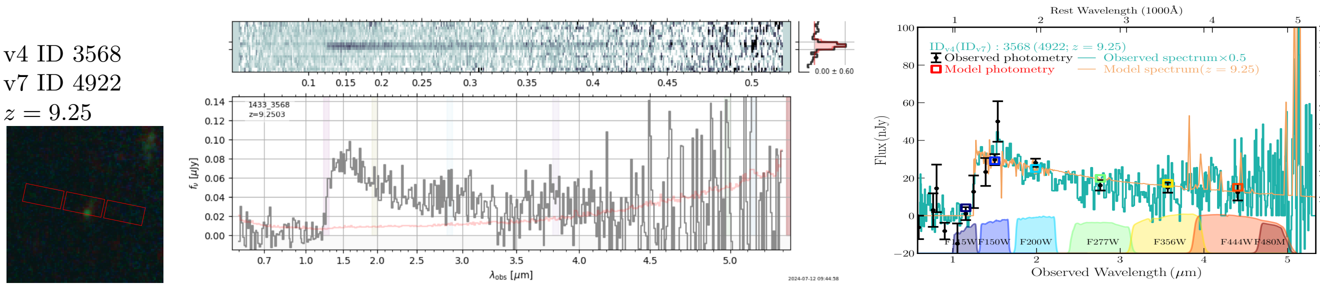

Figure 4. . Galaxy v4 3568 (v7 4922) at $z = 9.25$ with NIRSpec PRISM, reported previously by (Yanagisawa et al. 2024) and dubbed EBG-1 (Extremely Blue Galaxy). The source is modestly magnified by the foreground cluster, with $\mu = 2.72^{+0.09}_{-0.09}$. **Left:** NIRCam color images with slits overlaid. **Middle:** 2D and 1D spectra from DJA v3. **Right:** NIRCam photometry and SED fit with NIRSpec spectrum scaled to match.

3 and 8). This confirms the significant overdensity of $z \sim 6$ galaxies reported previously in *HST* observations of MACS0647 that was much higher than found behind other galaxy clusters (Bradley et al. 2014).

We note the photometric redshifts of these galaxies are slightly higher, $6.5 < z < 6.9$, as estimated previously (Bradley et al. 2014) based on *HST* images and again now with the addition of *JWST* images. Such slight overestimates have been reported previously (Heintz et al. 2025b; Hainline et al. 2024a; Fujimoto et al. 2023) and are attributed primarily to damped Lyα wings not accounted for in photometric redshift fitting codes. Roughly 20 galaxy candidates within our catalog fall in this range for photometric redshifts.

We further find that some of the $z \sim 6$ candidates presented in the *HST* analysis turn out to be more likely at the cluster redshift $z = 0.584$. This is due to a photometric redshift degeneracy: the cluster elliptical red rising SED can sometimes appear more like a high-z Lyman break in noisy *HST* photometric data for galaxies with mag ~ 27 and fainter (Song et al. 2012). This degeneracy is resolved by higher SNR *JWST* data extending to longer wavelengths.

Possible explanations for the observed overdensity include the presence of a forming protocluster or a large-scale structure along the line of sight (Jiang et al. 2018; Franck & McGaugh 2016). However, the lack of strong Lyα emission from multiple galaxies in the overdensity makes it difficult to conclusively identify it as a protocluster (Jiang et al. 2018; Bacon et al. 2021). Alternatively, cosmic variance or projection effects could also contribute to the apparent concentration of galaxies at this redshift (Franck & McGaugh 2016; Shi et al. 2019). Further spectroscopic confirmation, particularly of Lyα emission and velocity dispersion, will be necessary to distinguish between these scenarios.

4.5. *Little Red Dots*

We identify several Little Red Dots (LRDs) in this field. One was reported previously at $z = 4.53$ (Killi et al. 2024) based on the Cycle 1 NIRCam and NIRSpec PRISM data. This object (v4 1045) has broad Hα, a signature of AGN accretion disk broad line regions, with an estimated black hole mass $8 \times 10^8 M_\odot$. The photometry and spectra exhibit two components, including high dust attenuation $A_V > 5$ at longer wavelength, as found in other LRDs. Our Cycle 2 NIRSpec G395H data confirms the redshift and other properties.

Additionally, 1 arcmin away, our G395H spectrum of a $z \sim 6.5$ candidate v4 461 (v7 556) reveals it to be an LRD candidate at $z = 4.77$ with faint detections of [O III] and Hα (not shown); the detected lines are narrow, with no evidence for significant broadening.

Our Cycle 1 PRISM data also reveals a $z \sim 7.5$ candidate v4 1742 (v7 2193) to be an LRD candidate at $z = 5.81$. With the low resolution PRISM data, we do not detect significant broadening. The line is not clearly resolved with a upper limit width of ∼1000 km/s. But we do find that an additional broad component ∼4000 km/s significantly improves the fit. This may hint at the presence of an AGN.

4.6. *Lensing and Magnification*

MACS0647 is a well-studied strong-lensing cluster with several published mass models (e.g., Zitrin et al. 2011; Coe et al. 2013; Nishida et al. 2025). The depth and resolution of JWST reveal additional faint lensed sources as well as substructure within previously known images, enabling more precise lensing constraints.

Several of our high-redshift candidates correspond to systems identified in prior lensing analyses (Welch et al. 2022a; Meena et al. 2023). We list the matching IDs in Tables 3–4, providing a direct connection to existing mass-model constraints. Identifying these associations is essential for avoiding double counting in number-density estimates and for interpreting the intrinsic properties of these galaxies (Barkana & Loeb 2000; Lotz et al. 2017).

Table 2. Physical properties of spec-z confirmed galaxies derived from BAGPIPES NIRSpec PRISM line flux fitting. **Note:** Little Red Dots (LRDs) are marked with an asterisk (*); their SED fits may be unreliable due to extreme colors or AGN contamination.

ID (v7)	ID (v4)	$z_{\rm spec}$	Stellar Mass ($\log(M_*/M_\odot)$)	SFR (M_*/yr)	A_V (mag)	Mass-weighted Age (Gyr)
4922	3568	9.25	$7.80^{+0.25}_{-0.25}$	$2.85^{+0.58}_{-0.37}$	$0.01^{+0.01}_{-0.02}$	$0.01^{+0.01}_{-0.02}$
5191	3754	7.47	$8.30^{+0.03}_{-0.04}$	$20.19^{+1.47}_{-1.82}$	$0.04^{+0.02}_{-0.03}$	$0.00^{+0.00}_{-0.00}$
5591	3989	6.14	$8.05^{+0.23}_{-0.14}$	$0.66^{+0.17}_{-0.28}$	$0.16^{+0.10}_{-0.14}$	$0.15^{+0.09}_{-0.10}$
2121	1715	6.14	$8.14^{+0.20}_{-0.24}$	$3.26^{+0.70}_{-0.85}$	$0.06^{+0.03}_{-0.06}$	$0.03^{+0.02}_{-0.04}$
4533	3308	6.13	$7.72^{+0.03}_{-0.04}$	$5.32^{+0.32}_{-0.51}$	$0.10^{+0.03}_{-0.04}$	$0.00^{+0.00}_{-0.00}$
4411	3208	6.12	$8.93^{+0.09}_{-0.09}$	$15.89^{+2.06}_{-2.31}$	$0.11^{+0.03}_{-0.04}$	$0.04^{+0.01}_{-0.02}$
2193*	1742	5.81	$9.56^{+0.17}_{-0.07}$	$205.30^{+65.46}_{-47.51}$	$0.94^{+0.14}_{-0.06}$	$0.01^{+0.00}_{-0.00}$
1658	1395	3.72	$8.93^{+0.10}_{-0.05}$	$1.95^{+0.33}_{-0.51}$	$0.23^{+0.08}_{-0.11}$	$0.38^{+0.13}_{-0.13}$
4870	3533	3.23	$8.25^{+0.05}_{-0.05}$	$2.94^{+0.13}_{-0.17}$	$0.00^{+0.00}_{-0.01}$	$0.05^{+0.01}_{-0.01}$

Magnification factors for all candidates were computed using the mass model presented in (Nishida et al. 2025) that uses 86 multiple images from 28 sources to construct the mass model with GLAFIC Oguri (2010, 2021). Most galaxies lie outside the critical regions and therefore experience only mild magnification ($\mu \approx 1$–2) while a smaller subset located closer to the critical curves exhibit substantially higher values. Among the spectroscopically confirmed sources, the most magnified is ID 5931 ($z_{\rm spec} = 6.12$) with $\mu \approx 7.4$. The highest magnification in the full sample is ID 5595, which reaches $\mu \approx 11$, consistent with previous analyses of MACS0647.

These magnification estimates are used when reporting intrinsic luminosities and for comparing to luminosity functions. While the majority of our sample is only weakly affected by lensing, the most highly magnified systems provide valuable leverage for probing intrinsically faint galaxies and represent the dominant sources of model-dependent systematic uncertainty in our analysis (Meneghetti et al. 2017; Cerny et al. 2018).

4.7. *Low Redshift Interlopers*

Notably, we also find two high-redshift candidates ($z > 11$) turn out to be low-redshift interlopers ($z < 4$). The high-redshift estimates were based on SED fitting to the NIRCam DJA v4 catalog: $z \sim 12.3$ for v4 1395 (v7 1658) and $z \sim 11.4$ for v4 3533 (v7 4870). However, NIRSpec spectroscopy revealed significantly lower redshifts ($z_{\rm spec} = 3.72$ and 3.23) as shown in Fig. 5. Both galaxies have sharp Balmer breaks that were mistaken for high-redshift Lyman breaks, a classic degeneracy in photometric redshifts.

JWST photometry is often sufficiently precise to resolve such degeneracies. In fact, we found that updating from version 4 to version 7 NIRCam image reductions improved the photometric data, shifting the probability distribution to favor the lower redshift solutions. This illustrates how data reduction pipelines can influence redshift estimates as noted in Bagley et al. (2023). The full catalog, including both photometric and spectroscopic redshifts for all candidates, is provided in Appendix 7.

5. CONCLUSION

In this paper, we present a new catalog derived from JWST NIRCam and NIRSpec observations of the galaxy cluster MACS0647, revealing a diverse sample of 57 high-redshift galaxy candidates with $z > 6$. Spectroscopic observations with NIRSpec confirm redshifts for 14 of these candidates, offering a detailed look into galaxy assembly within the first billion years of cosmic history through their physical properties, from stellar masses and ages to star formation rates and dust content.

The spectroscopic confirmation of these high-redshift galaxies aligns with recent discoveries from other JWST programs, such as CEERS and JADES, which have identified and confirmed galaxies at redshifts $z > 10$ (Finkelstein et al. 2023; D'Eugenio et al. 2024). These collective efforts underscore the remarkable capability of JWST to probe the distant universe and enhance our understanding of the Epoch of Reionization.

The physical properties derived from our sample indicate a range of stellar masses and star formation rates, suggesting a wide-ranging population of early galaxies. This diversity is consistent with findings from the JADES program, which reported a variety of galaxy sizes and luminosities at similar redshifts (D'Eugenio et al. 2024). Such variations imply different evolutionary pathways and formation histories, offering valuable insights into the processes governing early galaxy assembly.

Notably, our results, alongside those from CEERS and other surveys, point to the prevalence of relatively low dust content in the majority of early-universe galaxies (Weaver et al. 2024; Hainline et al. 2024b; Windhorst et al. 2023). This suggests that significant dust production had yet to occur in many of these galaxies, which is consistent with the limited time available for dust formation and enrichment processes in the early universe.

In summary, our work expands the growing sample of spectroscopically confirmed high-redshift galaxies and reinforces the emerging picture of a diverse early galaxy population. The range of physical properties observed in MACS0647 highlights the complexity of galaxy assembly within the first billion years. Continued spectroscopic follow-up with JWST will be essential for refining these results and for connecting early galaxy populations to the progress of reionization.

6. ACKNOWLEDGMENTS

K.W. thanks the William H. Miller Graduate Fellowship and the MDSGC Observatory Fellowship. K.W. also thanks the LSST-DA Data Science Fellowship Program, which is funded by LSST-DA, the Brinson Foundation, and the Moore Foundation; his participation in the program has benefited this work.

This work is based on observations made with the NASA/ESA/CSA *JWST*. The *JWST* data presented in this article were obtained from the Mikulski Archive for Space Telescopes (MAST) at the Space Telescope Science Institute. The Association of Universities for Research in Astronomy (AURA), Inc. operates MAST under NASA contract NAS 5-03127 for *JWST*.

This work was supported by JSPS KAKENHI Grant Numbers JP25H00662, JP22K21349.

Software: grizli (Brammer et al. 2022), astropy (Astropy Collaboration et al. 2013, 2018, 2022), matplotlib (Hunter 2007), NumPy (Harris et al. 2020), SciPy (Virtanen et al. 2020), STScI *JWST* Calibration Pipeline (jwst-pipeline.readthedocs.io; Rigby et al. 2022, Bushouse et al. 2023), msaexp (Brammer 2023), PyNeb (Luridiana et al. 2014).

REFERENCES

Abdurro'uf, Larson, R. L., Coe, D., et al. 2024, ApJ, 973, 47, doi: 10.3847/1538-4357/ad6001

Adamo, A., Bradley, L. D., Vanzella, E., et al. 2024, Nature, 632, 513, doi: 10.1038/s41586-024-07703-7

Adams, N. J., Conselice, C. J., Ferreira, L., et al. 2023, MNRAS, 518, 4755, doi: 10.1093/mnras/stac3347

Arrabal Haro, P., Dickinson, M., Finkelstein, S. L., et al. 2023, arXiv e-prints, arXiv:2303.15431, doi: 10.48550/arXiv.2303.15431

Astropy Collaboration, Robitaille, T. P., Tollerud, E. J., et al. 2013, A&A, 558, A33, doi: 10.1051/0004-6361/201322068

Astropy Collaboration, Price-Whelan, A. M., Sipőcz, B. M., et al. 2018, AJ, 156, 123, doi: 10.3847/1538-3881/aabc4f

Astropy Collaboration, Price-Whelan, A. M., Lim, P. L., et al. 2022, ApJ, 935, 167, doi: 10.3847/1538-4357/ac7c74

Atek, H., Shuntov, M., Furtak, L. J., et al. 2023, MNRAS, 519, 1201, doi: 10.1093/mnras/stac3144

Bacon, R., Mary, D., Garel, T., et al. 2021, A&A, 647, A107, doi: 10.1051/0004-6361/202039887

Bagley, M. B., Finkelstein, S. L., Koekemoer, A. M., et al. 2023, ApJL, 946, L12, doi: 10.3847/2041-8213/acbb08

Barkana, R., & Loeb, A. 2000, ApJ, 531, 613, doi: 10.1086/308503

Bouwens, R. J., Illingworth, G. D., Oesch, P. A., et al. 2012, ApJL, 752, L5, doi: 10.1088/2041-8205/752/1/L5

Bouwens, R. J., Bradley, L., Zitrin, A., et al. 2014, ApJ, 795, 126, doi: 10.1088/0004-637X/795/2/126

Bradley, L. D., Zitrin, A., Coe, D., et al. 2014, ApJ, 792, 76, doi: 10.1088/0004-637X/792/1/76

Bradley, L. D., Coe, D., Brammer, G., et al. 2022, arXiv e-prints, arXiv:2210.01777, doi: 10.48550/arXiv.2210.01777

Brammer, G. 2023, msaexp: NIRSpec analysis tools (0.6.17), Zenodo, doi: 10.5281/zenodo.8319596

Brammer, G., Strait, V., Matharu, J., & Momcheva, I. 2022, grizli, 1.5.0, Zenodo, Zenodo, doi: 10.5281/zenodo.6672538

Brammer, G. B., van Dokkum, P. G., & Coppi, P. 2008, ApJ, 686, 1503, doi: 10.1086/591786

Bruzual, G., & Charlot, S. 2003, MNRAS, 344, 1000, doi: 10.1046/j.1365-8711.2003.06897.x

Buchner, J., Georgakakis, A., Nandra, K., et al. 2014, A&A, 564, A125, doi: 10.1051/0004-6361/201322971

Bushouse, H., Eisenhamer, J., Dencheva, N., et al. 2023, JWST Calibration Pipeline, 1.9.4, Zenodo, doi: 10.5281/zenodo.7577320

Cameron, A. J., Katz, H., Witten, C., et al. 2024, MNRAS, 534, 523, doi: 10.1093/mnras/stae1547

Carnall, A. C., McLure, R. J., Dunlop, J. S., & Davé, R. 2018, MNRAS, 480, 4379, doi: 10.1093/mnras/sty2169

Carnall, A. C., McLure, R. J., Dunlop, J. S., et al. 2019, MNRAS, 490, 417, doi: 10.1093/mnras/stz2544

Carniani, S., Hainline, K., D'Eugenio, F., et al. 2024, Nature, 633, 318, doi: 10.1038/s41586-024-07860-9

Casey, C. M., Akins, H. B., Shuntov, M., et al. 2023, arXiv e-prints, arXiv:2308.10932, doi: 10.48550/arXiv.2308.10932

Castellano, M., Fontana, A., Treu, T., et al. 2022, ApJL, 938, L15, doi: 10.3847/2041-8213/ac94d0

Castellano, M., Fontana, A., Merlin, E., et al. 2025, arXiv e-prints, arXiv:2504.05893, doi: 10.48550/arXiv.2504.05893

Cerny, C., Sharon, K., Andrade-Santos, F., et al. 2018, ApJ, 859, 159, doi: 10.3847/1538-4357/aabe7b

Claeyssens, A., Adamo, A., Richard, J., et al. 2023, MNRAS, 520, 2180, doi: 10.1093/mnras/stac3791

Coe, D., Zitrin, A., Carrasco, M., et al. 2013, ApJ, 762, 32, doi: 10.1088/0004-637X/762/1/32

Coe, D., Salmon, B., Bradač, M., et al. 2019, ApJ, 884, 85, doi: 10.3847/1538-4357/ab412b

Conroy, C., & Gunn, J. E. 2010, FSPS: Flexible Stellar Population Synthesis, Astrophysics Source Code Library, record ascl:1010.043. http://ascl.net/1010.043

Curtis-Lake, E., Carniani, S., Cameron, A., et al. 2023, Nature Astronomy, doi: 10.1038/s41550-023-01918-w

Dayal, P., & Ferrara, A. 2018, PhR, 780, 1, doi: 10.1016/j.physrep.2018.10.002

D'Eugenio, F., Cameron, A. J., Scholtz, J., et al. 2024, JADES Data Release 3 – NIRSpec/MSA spectroscopy for 4,000 galaxies in the GOODS fields. https://arxiv.org/abs/2404.06531

Donnan, C. T., McLeod, D. J., Dunlop, J. S., et al. 2023, MNRAS, 518, 6011, doi: 10.1093/mnras/stac3472

Donnan, C. T., McLure, R. J., Dunlop, J. S., et al. 2024, MNRAS, 533, 3222, doi: 10.1093/mnras/stae2037

Duncan, K., & Conselice, C. J. 2015, MNRAS, 451, 2030, doi: 10.1093/mnras/stv1049

Ebeling, H., Barrett, E., Donovan, D., et al. 2007, ApJL, 661, L33, doi: 10.1086/518603

Eifler, T., Miyatake, H., Krause, E., et al. 2021, MNRAS, 507, 1746, doi: 10.1093/mnras/stab1762

Fan, X., Strauss, M. A., Becker, R. H., et al. 2006, AJ, 132, 117, doi: 10.1086/504836

Feroz, F., & Hobson, M. P. 2008, MNRAS, 384, 449, doi: 10.1111/j.1365-2966.2007.12353.x

Feroz, F., Hobson, M. P., & Bridges, M. 2009, MNRAS, 398, 1601, doi: 10.1111/j.1365-2966.2009.14548.x

Feroz, F., & Skilling, J. 2013, in American Institute of Physics Conference Series, Vol. 1553, Bayesian Inference and Maximum Entropy Methods in Science and Engineering: 32nd International Workshop on Bayesian Inference and Maximum Entropy Methods in Science and Engineering, ed. U. von Toussaint, 106–113, doi: 10.1063/1.4819989

Finkelstein, S. L., Bagley, M. B., Arrabal Haro, P., et al. 2022, ApJL, 940, L55, doi: 10.3847/2041-8213/ac966e

Finkelstein, S. L., Bagley, M. B., Ferguson, H. C., et al. 2023, ApJL, 946, L13, doi: 10.3847/2041-8213/acade4

Franck, J. R., & McGaugh, S. S. 2016, ApJ, 817, 158, doi: 10.3847/0004-637X/817/2/158

Fujimoto, S., Arrabal Haro, P., Dickinson, M., et al. 2023, ApJL, 949, L25, doi: 10.3847/2041-8213/acd2d9

Fujimoto, S., Wang, B., Weaver, J. R., et al. 2024, ApJ, 977, 250, doi: 10.3847/1538-4357/ad9027

Furtak, L. J., Meena, A. K., Zackrisson, E., et al. 2024, MNRAS, 527, L7, doi: 10.1093/mnrasl/slad135

Gardner, J. P., Mather, J. C., Clampin, M., et al. 2006, SSRv, 123, 485, doi: 10.1007/s11214-006-8315-7

Goulding, A. D., Greene, J. E., Setton, D. J., et al. 2023, arXiv e-prints, arXiv:2308.02750, doi: 10.48550/arXiv.2308.02750

Hainline, K. N., Johnson, B. D., Robertson, B., et al. 2024a, ApJ, 964, 71, doi: 10.3847/1538-4357/ad1ee4

—. 2024b, ApJ, 964, 71, doi: 10.3847/1538-4357/ad1ee4

Harikane, Y., Nakajima, K., Ouchi, M., et al. 2023, arXiv e-prints, arXiv:2304.06658, doi: 10.48550/arXiv.2304.06658

Harikane, Y., Inoue, A. K., Mawatari, K., et al. 2022, ApJ, 929, 1, doi: 10.3847/1538-4357/ac53a9

Harris, C. R., Millman, K. J., van der Walt, S. J., et al. 2020, Nature, 585, 357, doi: 10.1038/s41586-020-2649-2

Heintz, K. E., Watson, D., Brammer, G., et al. 2023, arXiv e-prints, arXiv:2306.00647, doi: 10.48550/arXiv.2306.00647

—. 2024, Science, 384, 890, doi: 10.1126/science.adj0343

Heintz, K. E., Brammer, G. B., Watson, D., et al. 2025a, A&A, 693, A60, doi: 10.1051/0004-6361/202450243

—. 2025b, A&A, 693, A60, doi: 10.1051/0004-6361/202450243

Hsiao, T. Y.-Y., Coe, D., Abdurro'uf, et al. 2023a, ApJL, 949, L34, doi: 10.3847/2041-8213/acc94b

Hsiao, T. Y.-Y., Abdurro'uf, Coe, D., et al. 2023b, arXiv e-prints, arXiv:2305.03042, doi: 10.48550/arXiv.2305.03042

Hsiao, T. Y.-Y., Topping, M. W., Coe, D., et al. 2024, arXiv e-prints, arXiv:2409.04625, doi: 10.48550/arXiv.2409.04625

Hunter, J. D. 2007, Computing in Science & Engineering, 9, 90, doi: 10.1109/MCSE.2007.55

Jiang, L., Wu, J., Bian, F., et al. 2018, Nature Astronomy, 2, 962, doi: 10.1038/s41550-018-0587-9

Killi, M., Watson, D., Brammer, G., et al. 2024, A&A, 691, A52, doi: 10.1051/0004-6361/202348857

Kokorev, V., Atek, H., Chisholm, J., et al. 2025, ApJL, 983, L22, doi: 10.3847/2041-8213/adc458

Kroupa, P. 2002, Science, 295, 82, doi: 10.1126/science.1067524

Leja, J., Carnall, A. C., Johnson, B. D., Conroy, C., & Speagle, J. S. 2019, ApJ, 876, 3, doi: 10.3847/1538-4357/ab133c

Loeb, A., & Barkana, R. 2001, ARA&A, 39, 19, doi: 10.1146/annurev.astro.39.1.19

Lotz, J. M., Koekemoer, A., Coe, D., et al. 2017, ApJ, 837, 97, doi: 10.3847/1538-4357/837/1/97

Luridiana, V., Morisset, C., & Shaw, R. A. 2014, Astronomy & Astrophysics, 573, A42, doi: 10.1051/0004-6361/201323152

McKinney, J., Finnerty, L., Casey, C. M., et al. 2023, ApJL, 946, L39, doi: 10.3847/2041-8213/acc322

Meena, A. K., Zitrin, A., Jiménez-Teja, Y., et al. 2023, ApJL, 944, L6, doi: 10.3847/2041-8213/acb645

Mellier, Y., & et al. 2025, Astronomy & Astrophysics, 697, A1, doi: 10.1051/0004-6361/202450810

Meneghetti, M., et al. 2017, Mon. Not. Roy. Astron. Soc., 472, 3177, doi: 10.1093/mnras/stx2064

Meštrić, U., Vanzella, E., Zanella, A., et al. 2022, MNRAS, 516, 3532, doi: 10.1093/mnras/stac2309

Mobasher, B., Dahlen, T., Ferguson, H. C., et al. 2015, ApJ, 808, 101, doi: 10.1088/0004-637X/808/1/101

Mowla, L., Iyer, K., Asada, Y., et al. 2024, Nature, 636, 332, doi: 10.1038/s41586-024-08293-0

Naidu, R. P., Tacchella, S., Mason, C. A., et al. 2020, ApJ, 892, 109, doi: 10.3847/1538-4357/ab7cc9

Naidu, R. P., Oesch, P. A., van Dokkum, P., et al. 2022a, ApJL, 940, L14, doi: 10.3847/2041-8213/ac9b22

Naidu, R. P., Oesch, P. A., Setton, D. J., et al. 2022b, arXiv e-prints, arXiv:2208.02794, doi: 10.48550/arXiv.2208.02794

Naidu, R. P., Oesch, P. A., van Dokkum, P., et al. 2022c, ApJL, 940, L14, doi: 10.3847/2041-8213/ac9b22

Naidu, R. P., Oesch, P. A., Brammer, G., et al. 2025, arXiv e-prints, arXiv:2505.11263, doi: 10.48550/arXiv.2505.11263

Nakajima, K., Ouchi, M., Isobe, Y., et al. 2023, ApJS, 269, 33, doi: 10.3847/1538-4365/acd556

Nightingale, J. W., Mahler, G., McCleary, J., et al. 2025, MNRAS, 543, 203, doi: 10.1093/mnras/staf1253

Nishida, S., Oguri, M., Fudamoto, Y., & Kitamura, A. 2025, The Open Journal of Astrophysics, 8, 123, doi: 10.33232/001c.141938

Oguri, M. 2010, PASJ, 62, 1017, doi: 10.1093/pasj/62.4.1017

—. 2021, PASP, 133, 074504, doi: 10.1088/1538-3873/ac12db

Pacifici, C., Kassin, S. A., Weiner, B., Charlot, S., & Gardner, J. P. 2013, ApJL, 762, L15, doi: 10.1088/2041-8205/762/1/L15

Papovich, C., Finkelstein, S. L., Ferguson, H. C., Lotz, J. M., & Giavalisco, M. 2011, MNRAS, 412, 1123, doi: 10.1111/j.1365-2966.2010.17965.x

Pérez-González, P. G., Östlin, G., Costantin, L., et al. 2025, ApJ, 991, 179, doi: 10.3847/1538-4357/adf8c9

Postman, M., Coe, D., Benítez, N., et al. 2012, ApJS, 199, 25, doi: 10.1088/0067-0049/199/2/25

Rhoads, J. E., Wold, I. G. B., Harish, S., et al. 2023, ApJL, 942, L14, doi: 10.3847/2041-8213/acaaaf

Rigby, J., Perrin, M., McElwain, M., et al. 2022, arXiv e-prints, arXiv:2207.05632. https://arxiv.org/abs/2207.05632

Robertson, B. E. 2022, ARA&A, 60, 121, doi: 10.1146/annurev-astro-120221-044656

Sanders, R. L., Shapley, A. E., Topping, M. W., Reddy, N. A., & Brammer, G. B. 2023, ApJ, 955, 54, doi: 10.3847/1538-4357/acedad

Shi, K., Huang, Y., Lee, K.-S., et al. 2019, ApJ, 879, 9, doi: 10.3847/1538-4357/ab2118

Smit, R., Bouwens, R. J., Labbé, I., et al. 2014, ApJ, 784, 58, doi: 10.1088/0004-637X/784/1/58

Song, J., Mohr, J. J., Barkhouse, W. A., et al. 2012, ApJ, 747, 58, doi: 10.1088/0004-637X/747/1/58

Tang, M., Stark, D. P., Ellis, R. S., et al. 2024, MNRAS, 531, 2701, doi: 10.1093/mnras/stae1338

Vanzella, E., Castellano, M., Bergamini, P., et al. 2022, A&A, 659, A2, doi: 10.1051/0004-6361/202141590

Virtanen, P., Gommers, R., Oliphant, T. E., et al. 2020, Nature Methods, 17, 261, doi: 10.1038/s41592-019-0686-2

Wang, B., Fujimoto, S., Labbe, I., et al. 2023, arXiv e-prints, arXiv:2308.03745, doi: 10.48550/arXiv.2308.03745

Weaver, J. R., Cutler, S. E., Pan, R., et al. 2024, ApJS, 270, 7, doi: 10.3847/1538-4365/ad07e0

Welch, B., Coe, D., Zitrin, A., et al. 2022a, arXiv e-prints, arXiv:2207.03532. https://arxiv.org/abs/2207.03532

Welch, B., Coe, D., Diego, J. M., et al. 2022b, Nature, 603, 815, doi: 10.1038/s41586-022-04449-y

Welch, B., Coe, D., Zackrisson, E., et al. 2022c, ApJL, 940, L1, doi: 10.3847/2041-8213/ac9d39

Whitler, L., Endsley, R., Stark, D. P., et al. 2023, MNRAS, 519, 157, doi: 10.1093/mnras/stac3535

Windhorst, R. A., Cohen, S. H., Jansen, R. A., et al. 2023, AJ, 165, 13, doi: 10.3847/1538-3881/aca163

Wu, Z., Eisenstein, D. J., Johnson, B. D., et al. 2025, ApJ, 992, 212, doi: 10.3847/1538-4357/ae01a1

Yan, H., Ma, Z., Ling, C., Cheng, C., & Huang, J.-S. 2023, ApJL, 942, L9, doi: 10.3847/2041-8213/aca80c

Yanagisawa, H., Ouchi, M., Nakajima, K., et al. 2024, arXiv e-prints, arXiv:2411.19893. https://arxiv.org/abs/2411.19893

Zheng, W., Postman, M., Zitrin, A., et al. 2012, Nature, 489, 406, doi: 10.1038/nature11446

Zitrin, A., Broadhurst, T., Barkana, R., Rephaeli, Y., & Benítez, N. 2011, MNRAS, 410, 1939, doi: 10.1111/j.1365-2966.2010.17574.x

7. APPENDIX

7.1. *Full Candidate List*

Table 3. High-redshift candidates identified in this work, including cross-matches with Bradley et al. (2014) and Meena et al. (2023). Magnification factors are derived from the MACS0647 mass model of Nishida et al. (2025), constructed with GLAFIC (Oguri 2010, 2021), with 68% confidence intervals quoted. **Note:** Little Red Dots (LRDs) are marked with an asterisk (*); their SED fits may be unreliable due to extreme colors or AGN contamination.

ID(v7)	ID(v4)	Bradley 14 ID	Meena 24 ID	RA	DEC	F200W mag	$z_{\rm phot}$	$z_{\rm spec}$	μ
173	116	···	···	101.964896	70.184156	27.422	6.71	···	$1.10^{+0.01}_{-0.01}$
274	198	···	···	101.935274	70.185656	27.744	9.52	···	$1.06^{+0.01}_{-0.01}$
587	486	···	···	101.868833	70.189611	27.996	9.64	···	$1.02^{+0.01}_{-0.01}$
792	661	···	···	101.978383	70.19233	28.094	6.69	···	$1.14^{+0.01}_{-0.01}$
904	753	···	···	101.87733	70.193708	29.455	7.15	···	$1.03^{+0.01}_{-0.01}$
1021	852	···	···	101.96016	70.195471	29.895	6.70	···	$1.12^{+0.01}_{-0.01}$
1107	926	···	···	101.957695	70.196484	26.004	6.72	···	$1.12^{+0.01}_{-0.01}$
1133	946	···	···	101.950988	70.196883	29.287	6.83	···	$1.11^{+0.01}_{-0.01}$
1175	986	···	···	101.975962	70.197477	28.262	9.61	···	$1.17^{+0.01}_{-0.02}$
1352	1139	···	···	101.906024	70.19979	28.262	6.86	···	$1.06^{+0.01}_{-0.01}$
1471	1243	···	···	101.924964	70.201544	27.110	9.16	···	$1.08^{+0.02}_{-0.01}$
1626	1378	···	···	101.961021	70.203511	28.324	6.20	···	$1.16^{+0.01}_{-0.02}$
1658	1395	···	···	101.903143	70.203745	26.019	12.49	3.72	$1.06^{+0.01}_{-0.01}$
1857	1559	···	···	101.932349	70.206767	27.863	10.96	···	$1.12^{+0.02}_{-0.02}$
2120	1714	···	···	101.983563	70.209769	26.919	6.71	···	$1.26^{+0.02}_{-0.02}$
2121	1715	···	···	101.983171	70.209787	27.316	6.69	6.14	$1.26^{+0.02}_{-0.02}$
2193*	1742	···	···	101.892498	70.210177	26.400	7.54	5.81	$1.10^{+0.02}_{-0.01}$
2172	1751	···	···	101.971957	70.21037	27.197	9.00	···	$1.25^{+0.02}_{-0.02}$
2426	1882	···	···	101.944994	70.212959	29.287	6.82	···	$1.19^{+0.02}_{-0.02}$
2510	1912	···	···	101.977783	70.213676	27.291	6.69	···	$1.30^{+0.02}_{-0.02}$
2551	1924	···	···	101.902034	70.213857	25.843	9.58	···	$1.14^{+0.02}_{-0.02}$
2619	1944	···	···	101.986107	70.214346	25.715	6.12	···	$1.32^{+0.02}_{-0.02}$
2846	2019	···	···	101.973309	70.215423	27.744	6.82	···	$1.31^{+0.02}_{-0.02}$
4010	2876	2175	···	101.984019	70.229488	27.395	6.67	6.10	$1.80^{+0.04}_{-0.04}$
4213	3035	···	···	101.922863	70.234139	28.094	8.93	···	$1.78^{+0.06}_{-0.05}$
4268	3090	1976	···	101.954327	70.235365	26.444	6.31	6.13	$1.98^{+0.07}_{-0.06}$
4336	3138	···	···	101.906778	70.236517	27.175	7.03	···	$1.81^{+0.06}_{-0.05}$
4393	3186	···	···	101.971685	70.237378	28.797	8.90	···	$3.37^{+0.13}_{-0.14}$
4411	3208	···	···	101.918791	70.237614	26.422	6.58	6.12	$2.03^{+0.07}_{-0.07}$
4533	3308	···	16.4	101.952449	70.239294	27.395	6.70	6.13	$2.77^{+0.13}_{-0.11}$
4797	3493	···	···	101.920053	70.241989	27.707	10.02	···	$3.51^{+0.18}_{-0.17}$
4824	3504	···	···	101.903249	70.242103	29.895	8.36	···	$2.42^{+0.08}_{-0.08}$
4870	3533	···	15.1	101.999421	70.242449	25.515	11.41	3.23	$6.58^{+0.45}_{-0.37}$
4919	3567	···	5.2	101.9216	70.242932	27.175	6.91	···	$4.01^{+0.20}_{-0.20}$
4922	3568	···	···	101.90398	70.242978	27.782	9.57	9.25	$2.72^{+0.09}_{-0.09}$
5091	3643	···	···	101.97757	70.244199	27.707	6.10	···	$5.01^{+0.27}_{-0.27}$
5191	3754	1411	10.2	101.920529	70.244899	25.605	7.33	7.47	$7.51^{+0.44}_{-0.43}$
5595	3983	···	16.2	101.944871	70.248877	22.249	6.69	···	$10.97^{+3.67}_{-2.10}$
5591	3989	···	···	101.940754	70.249101	28.262	6.30	6.14	$1.99^{+0.10}_{-0.10}$
5594	3993	···	10.1	101.919592	70.24904	26.193	7.34	···	$6.78^{+0.40}_{-0.40}$

Table 4. High-redshift candidates identified in this work (Part 2), including cross-matches with Bradley et al. (2014) and Meena et al. (2023). Magnification values follow the same lens model described in Table 3.

ID(v7)	ID(v4)	Bradley 14 ID	Meena 24 ID	RA	DEC	F200W mag	$z_{\rm phot}$	$z_{\rm spec}$	μ
5881	4186	···	5.1	101.921109	70.251551	26.772	6.33	···	$4.60^{+0.24}_{-0.22}$
5931	4219	···	···	101.916697	70.252253	29.455	6.66	6.12	$7.41^{+0.63}_{-0.57}$
6339	4514	···	···	101.99504	70.255751	29.014	6.81	···	$2.92^{+0.10}_{-0.09}$
6736	4775	···	···	101.934471	70.259417	27.131	6.52	···	$6.78^{+0.19}_{-0.16}$
6839	4838	···	···	101.934269	70.260138	28.147	6.30	···	$3.74^{+0.19}_{-0.16}$
6871	4865	···	···	102.010301	70.260557	29.142	8.93	···	$1.87^{+0.05}_{-0.04}$
6901	4893	···	···	101.965589	70.26072	28.147	6.56	···	$2.11^{+0.10}_{-0.09}$
6941	4914	···	···	101.964944	70.260979	28.900	6.63	···	$2.09^{+0.09}_{-0.09}$
6943	4915	···	···	101.945294	70.261003	28.203	9.55	···	$2.93^{+0.15}_{-0.14}$
6952	4920	···	···	101.964462	70.261078	28.324	7.03	···	$2.10^{+0.09}_{-0.09}$
7120	5010	339	···	101.924688	70.261861	25.534	6.16	6.11	$2.63^{+0.09}_{-0.07}$
7193	5057	···	16.3	101.966915	70.262567	29.653	6.69	···	$1.89^{+0.08}_{-0.07}$
7282	5094	···	···	101.925405	70.263143	26.467	7.37	7.00	$2.32^{+0.07}_{-0.06}$
7397	5156	···	···	101.972484	70.264076	29.142	9.38	···	$1.68^{+0.06}_{-0.06}$
7576	5332	···	···	101.963323	70.265634	28.324	7.28	···	$1.60^{+0.05}_{-0.05}$
7604	5352	···	···	101.98205	70.26602	27.509	6.70	···	$1.51^{+0.05}_{-0.04}$
7697	5420	···	···	101.922465	70.266946	27.672	6.56	···	$1.84^{+0.05}_{-0.04}$

7.2. *NIRSpec Fluxes and Spectra*

Table 5. Emission line fluxes (1e-20 cgs) measured for galaxies observed with NIRSpec PRISM.

ID(v7)	1658	2121	2193	4411	4533	4870	4922	5191	5591
OII	89±21	26±8	...	91±14	110±8	...	...	21±5	...
HeI-3889	87±19	...	...	...	36±9	...	...	23±6	...
Ha+NII	150±7	106±7	994±16	123±9	454±9	245±10	...	...	43±5
SII	18±5	...	...	...	21±4	...	...	...	...
HeI-7065	16±5	...	...	...	...	...	...	...	13±4
SIII-9531	17±5	...	...	...	...	25±6	...	...	...
OIII-1663	...	155±40	...	...	...	...	...	...	...
OIII-4363	...	26±6	...	...	27±6	...	...	14±4	...
Hb	...	34±5	214±10	47±8	206±7	87±15	18±5	70±5	...
OIII-4959	...	54±5	336±11	82±8	436±10	...	34±6	103±5	23±4
OIII-5007	414±15	184±7	908±18	241±10	1250±18	671±22	65±6	334±8	72±5
HeI-5877	...	...	37±6	...	20±4	...	...	...	...
OII-7325	...	...	...	31±10	...	...	...	...	...
NeIII-3867	...	...	...	50±16	56±9	...	...	22±6	...
NeIII-3968	...	...	...	...	52±7	...	...	24±5	...
Hd	...	...	...	...	64±6	...	...	28±6	...
Hg	...	...	...	...	100±7	...	...	24±4	...
HeI-1083	...	...	...	...	...	44±4	...	...	...
NIII-1750	...	...	...	...	...	...	88±27	...	...
12+log(O/H)		7.58 ± 0.27		8.14 ± 0.08	7.82 ± 0.10			7.50 ± 0.18	
12+log(O/H)[a]	$\sim$8.00[b]	7.61 ± 0.16	7.43 ± 0.03	7.57 ± 0.17	7.74 ± 0.05	$\sim$8.00[b]	7.33 ± 0.21	7.51 ± 0.06	> 7.67[c]
log(U)		-2.02 ± 0.06		-2.41 ± 0.07	-1.89 ± 0.13			-1.79 ± 0.15	

Note— [a] Derived from strong lines (i.e., R3 = OIII / Hβ) adopting the relation from Nakajima et al. (2023). [b] R3 is higher than the peak of the relation. [c] Lower limit from 3σ of Hβ.

Table 6. Emission line fluxes (1e-20 cgs) and FWHM (km/s) measured for galaxies observed with NIRSpec high-res G395H.

ID	ID	z	Hβ	Hβ	[OIII]	[OIII]	[OIII]	[OIII]	Hα	Hα
v7	v4		4863	4863	4960	4960	5008	5008	6565	6565
			flux	FWHM	flux	FWHM	flux	FWHM	flux	FWHM
5191	3754	7.466	231 ± 60	152^{+63}_{-42}	335 ± 59	143^{+35}_{-27}	1100 ± 79	128^{+12}_{-11}	...	...
7282	5094	6.999	...	...	388 ± 23	202^{+14}_{-13}	1067 ± 38	182^{+50}_{-48}	...	...
4268	3090	6.127	97 ± 13	157^{+28}_{-24}	197 ± 9	158 ± 8	638 ± 19	157 ± 5	366 ± 38	155^{+20}_{-17}
5931	4219	6.117	29 ± 7	104^{+35}_{-34}	43 ± 2	102 ± 5	180 ± 10	126^{+8}_{-7}	90 ± 24	105^{+43}_{-29}
7120	5010	6.115	1670 ± 168	213^{+23}_{-22}	3842 ± 231	193 ± 8	12460 ± 758	197 ± 9	4881 ± 301	172^{+11}_{-10}
4010	2876	6.101	43 ± 5	153^{+22}_{-19}	76 ± 4	166 ± 8	240 ± 11	172 ± 8	160 ± 33	161^{+48}_{-33}
2193	1742	5.797	133 ± 15	152 ± 16	373 ± 30	148^{+11}_{-10}	1059 ± 56	160^{+7}_{-6}	...	...

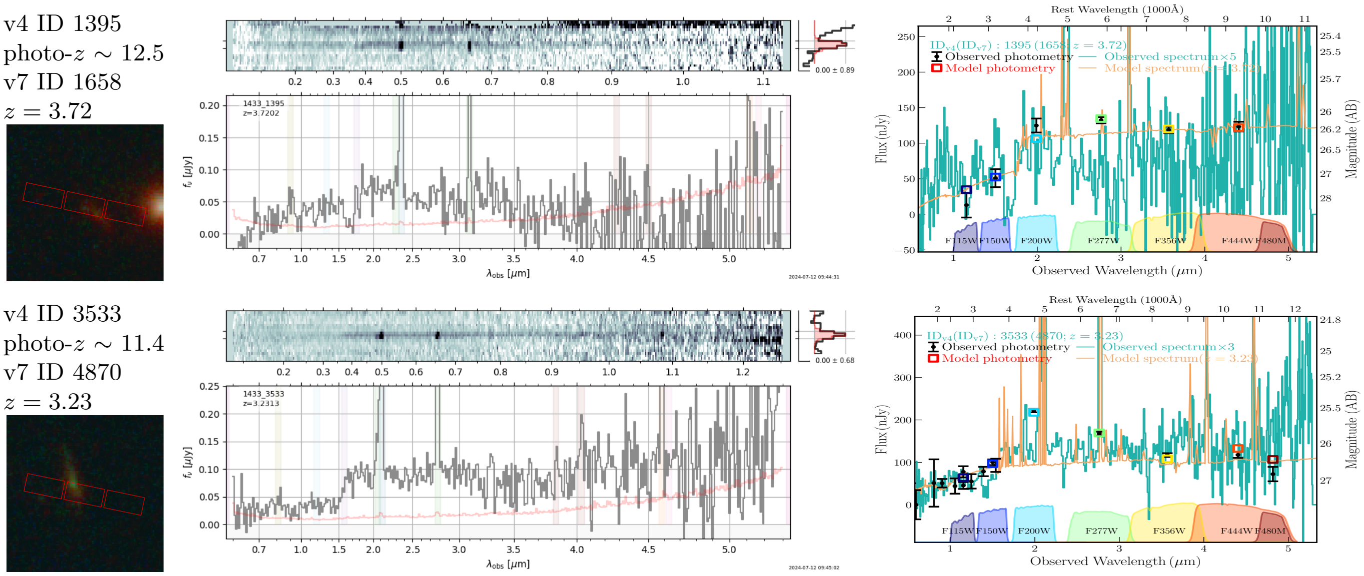

Figure 5. Candidate $z > 11$ galaxies (based on our NIRCam v4 photometry) shown to be interlopers at $z < 4$ with NIRSpec PRISM spectroscopy. In both cases, Balmer breaks are mistaken for Lyman breaks. **Top:** In the case of v4 3533 (v7 4870), strong emission lines [O III] and Hα conspire with the $z = 3.23$ Balmer break to mimic a blue SED ($\beta < -2$) with a Lyman break at $z \sim 11$. **Bottom:** Emission lines do not significantly affect the photometry of v4 1395 (v7 1658). A faint detection in F150W blueward of the break was missed in the v4 photometric catalog, then detected in the v7 catalog.

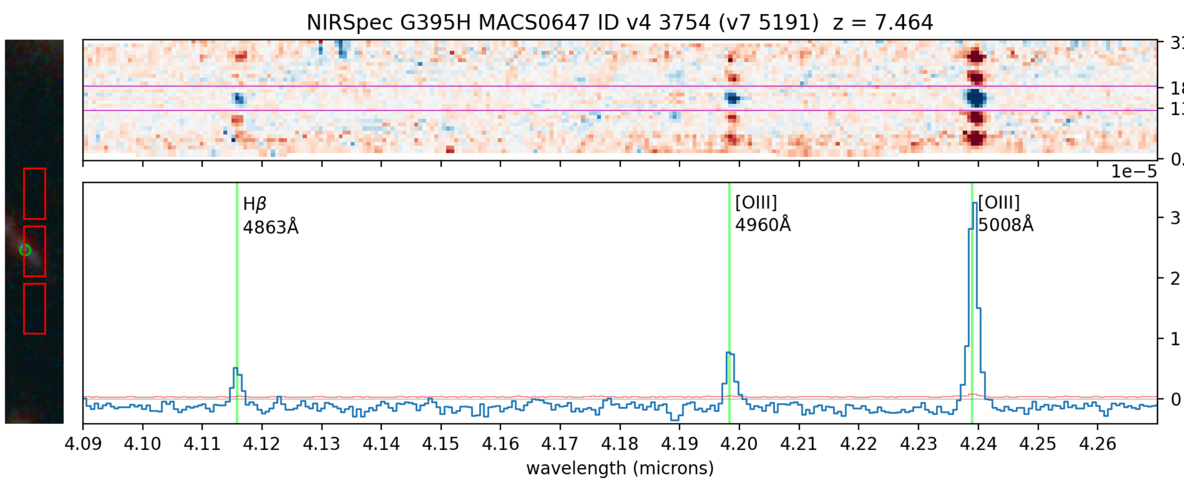

Figure 6. NIRSpec G395H high-resolution spectrum of galaxy v4 3754 (v7 5191) at $z = 7.464$, showing resolved Hβ, [O III], and Hα. The full 2.9–5.0 μm range also covers [O II] $\lambda\lambda$3727, which is not detected, consistent with the galaxy's high excitation.

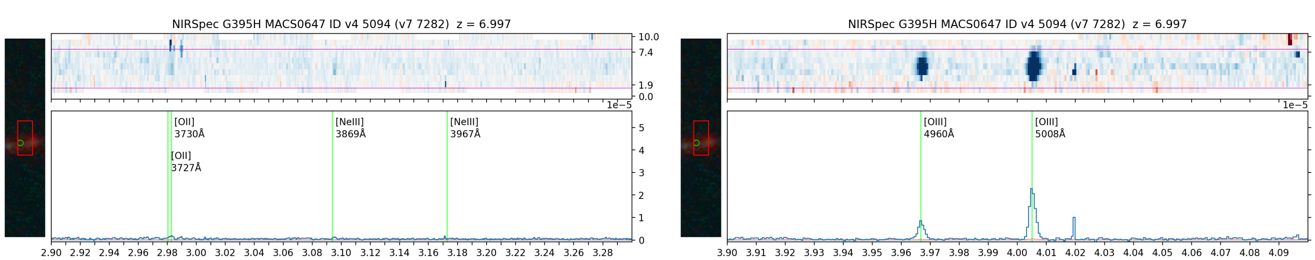

Figure 7. NIRSpec G395H spectrum of galaxy v4 5494 (v7 7282) at $z = 6.997$, with clear detections of Hβ, [O III], and Hα. The strong [O III] emission indicates a highly ionized, low-metallicity ISM typical of $z \sim 7$ galaxies.

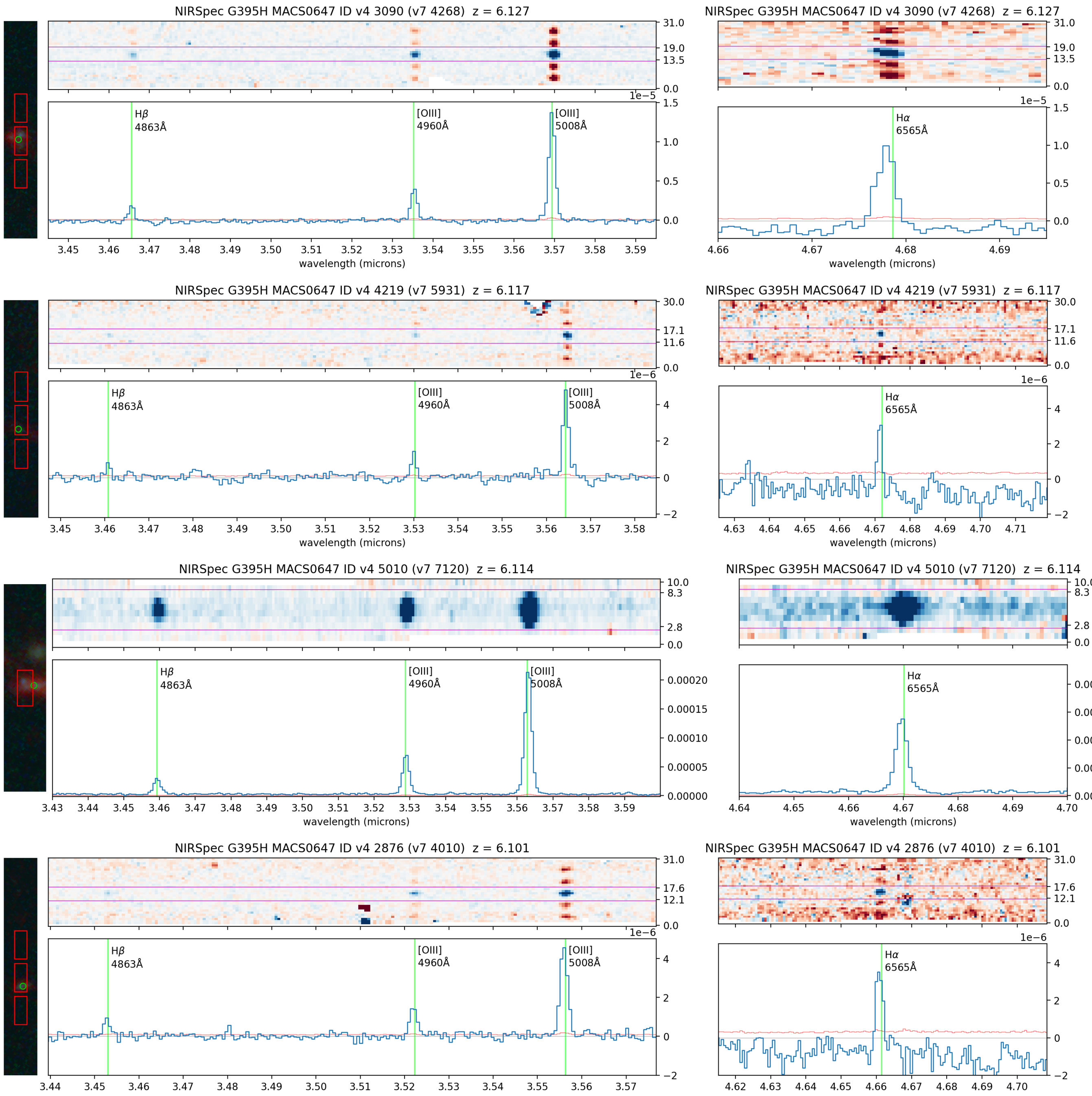

Figure 8. NIRSpec G395H high-resolution spectra of 4 galaxies that are part of our observed overdensity at $6.10 < z < 6.13$ showing Hβ, [O III], and Hα. Note that v4 3090 (v7 4268) consists of two components separated by ∼1 kpc and ∼90 km/s, suggesting a dynamical mass $\sim 10^8 M_\odot$.